Monthly Notices
of the
ROYAL ASTRONOMICAL SOCIETY
MNRAS **454,** 4159–4171 (2015) doi:10.1093/mnras/stv2257

High-precision photometry for *K2* Campaign 1

C. X. Huang,[1]★ K. Penev,[1] J. D. Hartman,[1] G. Á. Bakos,[1]†‡ W. Bhatti,[1] I. Domsa[2] and M. de Val-Borro[1]

[1]*Department of Astrophysical Sciences, Princeton University, Princeton, NJ 08544, USA*
[2]*Hungarian Astronomical Association, Budapest, H-1300, PO. Box 148, Hungary*

Accepted 2015 September 28. Received 2015 September 25; in original form 2015 July 27

ABSTRACT

The two reaction wheel *K2* mission promises and has delivered new discoveries in the stellar and exoplanet fields. However, due to the loss of accurate pointing, it also brings new challenges for the data reduction processes. In this paper, we describe a new reduction pipeline for extracting high-precision photometry from the *K2* data set, and present public light curves for the *K2* Campaign 1 target pixel data set. Key to our reduction is the derivation of global astrometric solutions from the target stamps, from which accurate centroids are passed on for high-precision photometry extraction. We extract target light curves for sources from a combined UCAC4 and EPIC catalogue – this includes not only primary targets of the *K2* campaign 1, but also any other stars that happen to fall on the pixel stamps. We provide the raw light curves, and the products of various detrending processes aimed at removing different types of systematics. Our astrometric solutions achieve a median residual of ∼0.127 arcsec. For bright stars, our best 6.5 h precision for raw light curves is ∼20 parts per million (ppm). For our detrended light curves, the best 6.5 h precision achieved is ∼15 ppm. We show that our detrended light curves have fewer systematic effects (or trends, or red-noise) than light curves produced by other groups from the same observations. Example light curves of transiting planets and a Cepheid variable candidate, are also presented. We make all light curves public, including the raw and detrended photometry, at http://k2.hatsurveys.org.

Key words: methods: data analysis – techniques: photometric – surveys – astrometry.

1 INTRODUCTION

The *Kepler* spacecraft ended its primary mission after the failure of two reaction wheels. The *K2* mission uses the *Kepler* spacecraft to perform 80-d observations of selected fields in the ecliptic plane. This brings new opportunities to study transiting planets around different stellar populations compared to the original *Kepler* field, such as clusters of young and pre-main sequence stars (Howell et al. 2014).

K2 uses the remaining two reaction wheels, and solar radiation pressure, to maintain close to constant pointing of the spacecraft over the 80-d per-field observations. Currently, observations are performed with 21 modules, each module consisting of 4 CCD channels, yielding 76 channels (2 modules failed). Due to the limited bandwidth, only postage stamps containing proposed targets are downloaded. These postage stamps are typically 25 × 25 pixels in size (depending on the brightness of the targets and campaigns). These make up only less than 10 per cent per cent of the entire field of view (FOV). The majority of stamps are observed at ∼ 30 min cadence. Typically, two Full Field Images (FFIs) are downloaded for the beginning and the end of campaign.

However, the two reaction wheel mode also brings in new challenges for the data reduction processes. The spacecraft pointing is less stable compared to the primary mission, leading to a potential decrease in the photometric precision. Although the disturbance from the solar pressure is mostly controlled by the two reaction wheels and the thruster firing (every 2 d), there is still a low-frequency motion remaining, resulting in the targets drifting across the FOV. The extracted aperture photometry light curves are dominated by the systematics induced by this drift pattern. Vanderburg & Johnson (2014, hereafter VA14) minimized this drift systematic by decorrelating the light curves with the motion of the spacecraft. They achieved a photometric precision that is within a factor of 2 of the original *Kepler* photometry. Various other teams also developed their own tools to reduce the *K2* data. Aigrain et al. (2015) used aperture photometry and a semi-parametric Gaussian process model to extract photometry from the *K2* engineering data. Lund et al. (2015) presented K2P, a pipeline specifically designed for astrometric analyses. Foreman-Mackey et al. (2015) and Angus,

★ E-mail: xuhuang@princeton.edu
† Sloan Fellow.
‡ Packard Fellow.

Foreman-Mackey & Johnson (2015) proposed a method to analysis the *K2* data without a general detrending process.

There is, however, room for further improvements. VA14 reduction achieved the highest precision among all the past works, but only derived photometry for the proposed *Kepler* targets (not all targets falling on silicon), and are also known to have remaining systematic variations affected by the spacecraft roll (Angus et al. 2015). Aigrain et al. (2015) and Lund et al. (2015) derive photometry for all of the targets on silicon, but achieved slightly lower precision than VA14, especially for the bright stars. Here, we present a new reduction of the *K2* data drawing on techniques used in analysing data from ground-based surveys (e.g. Bakos et al. 2010).

We approach the *K2* pixel file reduction with the following steps: (1) improved astrometry for source centroiding and flux extraction; (2) photometric extraction for *all* the stars observed on the *K2* postage stamps; (3) removal of first-order systematics via a modified External Parameter Decorrelation (EPD) procedure (broadly similar to VA14); (4) further reduction of the shared systematic trends via an implementation of the Trend Filtering Algorithm (TFA) and semi-periodic stellar oscillations via cosine-filtering. The global astrometry step is key to this process – it minimizes the effect of spacecraft drift on the aperture photometry, and allows us to accurately model the spacecraft motion for further detrending.

In this paper, we describe our *K2* photometry pipeline and the high-precision light curves from the reduction of *K2* Campaign 1. We introduce our effort of deriving accurate astrometry for the *K2* observations, making use of the *K2* FFIs, and present a revised *K2* Campaign 1 target list in Section 2. In Section 3, we present our aperture photometry method. In Section 4, we revisit our detrending techniques and present our light curves at different detrending stages. In Section 5, we compare our photometry with that of other studies.

2 ASTROMETRY

2.1 Background

The first step of our reduction is to derive an accurate astrometric solution of the *K2* data. Despite its large pixel scale (∼4 arcsec) and point spread function (PSF) full width at half-maximum (5–6 arcsec), the original *Kepler* mission turned out to be a great tool for accurate astrometry itself because of its extremely high signal to noise photometry and stable pointing. Monet et al. (2010) reported a preliminary astrometric solution precision, from the first few months of *Kepler* data, to be 0.001 pixel, nominal 4 mas. This high astrometric precision, and high stability of the centroid position, enabled the high photometric precision of the *Kepler* primary mission.

Unlike the original *Kepler* Mission, the *K2* stars typically drift across the CCD plane at a speed of 1–3 per cent of a pixel every 30 min. Since the 30 min *K2* frame is composed of 270 short exposures of 6 s each, the final PSF is inevitably distorted, and neighbouring stars tend to become blended. Therefore, it is difficult to determine accurate centroids from source extraction alone. Thus, we use an external catalogue, namely the fourth United States Naval Observatory (USNO) CCD Astrograph Catalogue, UCAC4 (Zacharias et al. 2013), which has an astrometric precision of 15–100 mas, to derive good astrometric solutions for the *K2* frames.

A good astrometric solution does not only benefit the photometric precision, but also enable us to make maximal use of the *K2* observations. The *K2* campaigns observe targets proposed by the community, and each target was then assigned a stamp of size 20–50 pixels across. This stamp size is much bigger than the original *Kepler* stamp size. In addition to the target, many other sources are observed in a typical *K2* stamp. We provide position information and reduced light curves for all of the stars observed in the *K2* stamps. We anticipate an improved planet yield from this approach, due to the larger number of sources available, and the availability of the light curves of neighbouring stars, useful in blend analyses.

We first derive a general astrometric solution using the Kepler FFIs and our custom developed astrometry software used for HATNet. This general solution is then used as an initial guess for the remaining stamp observations. We stitch all the *K2* stamps together into a 'Sparse FFI' (SFFI), with the unobserved regions masked. We fit for an astrometric solution to the SFFI, which is assumed to be a low-order polynomial distortion from the FFI astrometric solution.

2.2 Astrometry standard catalogue

We use the UCAC4 catalogue (Zacharias et al. 2013) as our astrometry standard for deriving the astrometric solution. It contains over 113 million objects, and is complete down to magnitude $R = 16$.

The precision of coordinates provided by UCAC4 is ∼15–100 mas. UCAC4 catalogue also contains proper motion of ∼105 million stars, with errors around 1–10 mas yr^{-1}. Both the coordinates and proper motions are measured on the International Celestial Reference System (ICRS) at a mean epoch of 2000. We linearly corrected the coordinates based on the proper motions to epoch 2014. UCAC4 also contains Two Micron All-Sky Survey (2MASS; Skrutskie et al. 2006) photometry for around 110 million stars, and AAVSO Photometric All-Sky Survey (APASS) five-band (BVgri) photometry for over 51 million stars. For the stars in 2MASS but without APASS photometry, their *gri* band photometry are estimated using the 2MASS magnitudes. *BV* band magnitudes are adopted from the Tycho-2 catalogue where available, otherwise also estimated from 2MASS. We use the *B* and *V* magnitude to estimate the magnitude of stars in the *Kepler* band when needed.

2.3 Astrometry on the full frame image

The *Kepler* FFIs are divided into subimages by readout channels. There are 84 subimages for each FFI. Two of the CCD modules (8 channels altogether) failed during the *Kepler* main mission. The remaining 76 subimages were used to create the images from the 38 working CCDs (following the Kepler Instrument Handbook). We use FISTAR (Pál 2012) for source extraction. The uncertainties of the source extractor is about 0.07 pixels. This is estimated by comparing the extracted source positions on the two different FFIs taken from the Campaign 1. The relative shift and rotation between the two FFIs were taken into account by fitting a low-order polynomial to the two extracted source lists. We also experimented with other source extractors such as SEXTRACTOR (Bertin & Arnouts 1996), and all gave similar uncertainties.

The astrometric solution is provided by ANMATCH, a software routinely produces arcsecond precision astrometric solutions for the HATNet/HATSouth observations. ANMATCH first uses the engine of astrometry.net (Lang et al. 2010) for a low-order solution [third-order Simple Imaging Polynomial (SIP) tweak] to obtain an initial guess, then fits a third-order polynomial on a bigger matched list between the extracted source and the catalogue source to obtain the final solution.

The histogram of the residuals from the astrometric solution, for all 38 CCDs in the *K2* Campaign 1 FFIs, is plotted in black in

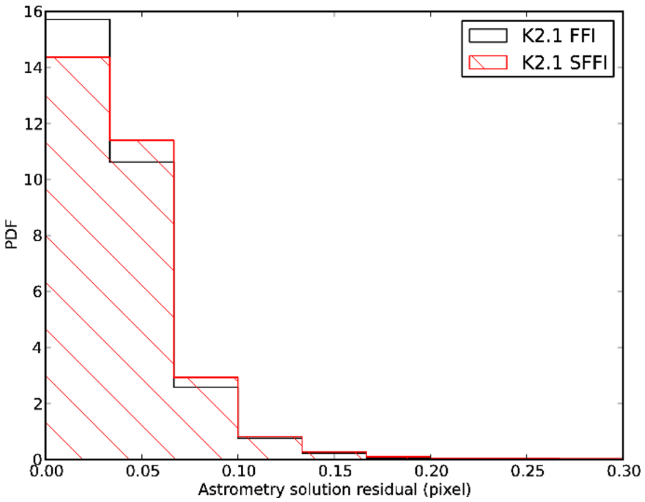

Figure 1. The residual of the astrometric solution for all channels of the *K2* Campaign 1 field FFIs (black) and SFFIs (red and hatched). This is computed by comparing the distance between the projected catalogue coordinates and the detected source coordinates on the CCDs.

Fig. 1. The astrometric solution residual is defined as the distance between the projected pixel coordinates of catalogue sources and the corresponding coordinates for the same stars from our source extractor. The median of the astrometric solution residual for these raw frames is ∼0.032 pixel for *K2* Campaign 1.[1] Given the *Kepler* CCD has a plate scale of 3.98 arcsec, our astrometric solution residual corresponds to 0.127 arcsec.

2.4 Astrometry for all the stamps

The SFFIs are very sparse. For a single channel, typically more than 95 per cent of the pixels are not downloaded. It is impossible to solve for the astrometric solution of these SFFIs via a direct catalogue matching. We use the FFI astrometric solution as an initial guess to overcome this problem.

We first use FISTAR to extract the sources from the SFFIs. We then project the UCAC4 catalogue on to the SFFIs with the astrometric solutions obtained in Section 2.3. We use an iterative point matching algorithm allowing a field centre shift from the FFI to SFFI to match the extracted sources and the projected coordinates of catalogue stars. We solve for the distortion between these matched pairs using a second-order polynomial to obtain the final solution. In Fig. 2, we show the corresponding region of FFI and SFFI from the same CCD channel (*K2* Campaign 1, module 13, channel 41). This region consists of three stamps in the SFFI observations. We marked out the detected source by cyan circles, and the projected sources from catalogue by red circles. The original *K2* targets are marked out in the black circles. Some stamps consist of multiple stars. We also show that in the top rightmost stamp in Fig. 2, the projected catalogue indicates that there are additional sources blended in the primary source's PSF, which was originally missed by the source extractor, and the light of which would be measured together with that of the primary source.

We compute our astrometric residuals as per Section 2.3. The astrometric residuals on the SFFIs for *K2* Campaign 1 are shown in red in Fig. 1. The median astrometric residual is around 0.034 pixels (0.135 arcsec), comparable with what we achieved on the FFIs.

2.5 A revised *K2* target catalogue

We projected the UCAC4 catalogue on the *K2* Campaign 1 SFFIs using the astrometric solution we obtained in Section 2.4. Stars with centroids within 3 pixels from the stamp edges were excluded. We also included those stars in the original Ecliptic Plane Input Catalogue (EPIC; Huber & Bryson 2015) but not in the UCAC4 catalogue. The EPIC catalogue is a combination of the *Hipparcos* catalogue (van Leeuwen 2007), Tycho-2 catalogue (Høg et al. 2000), UCAC4 catalogue, 2MASS, and SDSS DR9 (Ahn et al. 2012) for the selected *K2* target stars. There may be systematic offsets between the coordinates from the above catalogue, but they are relatively small (∼10 mas), and can be ignored when combining these catalogues. We estimated the *B* and *V* magnitudes of stars not in the EPIC catalogue as per the Kepler Instrument Handbook. Altogether, we found 14 778 stars from the UCAC4 catalogue, and an additional 7939 stars from the EPIC catalogue only, in *K2* Campaign 1. This combined set of *K2* target catalogue (22 717 stars in total) is larger by 5 per cent than the total in the original EPIC catalogue (21 647 stars in total). This increase will be more pronounced for other, more crowded *K2* fields. Part of the final *K2* Campaign 1 target list catalogue is shown in Table 1. We provide the centroid positions on the corresponding postage stamp, for each target.

2.6 The refined motion for each module

VA14 pointed out that the *K2* photometry is strongly correlated with the centroid positions of the stars. They also found that the centroid position of individual stars, as determined by their weighted light centres, are often not good enough. As such, they chose the centroid motion of a bright star to represent all the stars observed in the same campaign. Taking advantage of our derived astrometric solution, we find that by combining many stars observed on the same module, we can achieve even better constrained *X*,*Y* motion tracks. We define the *X*, *Y* motion derived for the centre pixel position of SFFI modules as the refined motion for each module. As an example, we show in Fig. 3 the relative *X* centroid drift of module 4, a module in the corner of the focal plane. We did not derive a rolling motion for the entire spacecraft to avoid correcting for additional rotations between modules. We notice that although the spacecraft attempted to correct its roll drift every 12 h, the drifting segments can last longer. The drifting segments are defined as a time series of smooth *X*, *Y* motion without significant outliers. We identify each drifting segment, and the outliers in between segments, by applying a 1D edge detection method (Sobel operator) on the *X* motion of each module. An example of the edge detection is show for module 4, in Fig. 3, with the red dashed lines separating each segment.

3 PHOTOMETRY

For each target, we use FIPHOT (Pál 2012) to extract photometry in 36 circular apertures around the derived centroids. The flux from the sources are estimated by summing up all the pixels within an aperture and weighting edge pixels by the fraction of which lie within the circular aperture. The background flux is measured by

[1] We expect a factor of 2 difference between the estimated uncertainties from the source extractor, and our astrometric residual, given the different methods by which these two uncertainties are calculated. We estimated the uncertainty of the source extractor by comparing the rms difference of the source positions on two frames (allowing a spacial transformation), while the uncertainty of the astrometric residual is estimated by the median of residual between the extracted position and the projected solution.

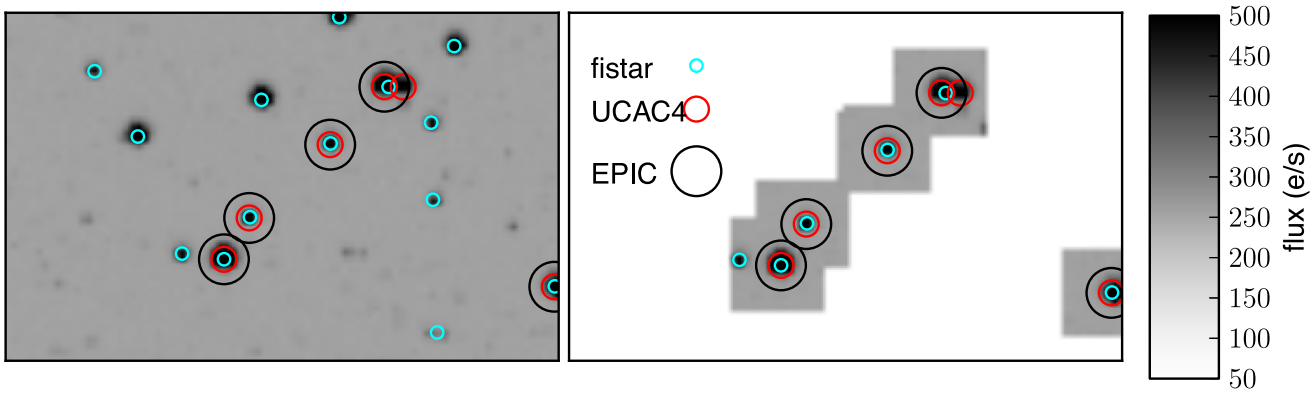

Figure 2. An 85 × 56 pixel^2 region of the FFI frame (left) and its corresponding SFFI frame (right). The detected sources are marked by cyan circles, and the projected sources from UCAC4 catalogue by red circles. The original *K2* targets are marked by black big circles centred on centroids as determined from our astrometric solution. The white region in the SFFI image were not observed, and are masked out.

Table 1. K2 target list.

UCAC4ID	RA	Dec.	J	H	K	B	V	g	r	i	x(t_0) [b]	y(t_0) [b]	channel [c]	K2ID [d]	flag[a]
UCAC4-555-033290	101.764 743	20.947 725	11.705	11.192	11.067	11.927	11.661	11.756	11.696	11.726	41.098 906	885.251 787	24	202071861	AAeeeAAAe
UCAC4-555-033327	101.789 413	20.952 493	14.487	12.700	12.157	15.417	14.481	14.920	14.144	13.857	42.030 470	863.957 681	24	202071849	AAeeeAAAe
UCAC4-555-033328	101.789 718	20.941 804	15.207	14.082	13.808	15.967	15.332	15.603	15.144	14.984	32.436 217	865.242 115	24	202071849	eeeeeeeee
UCAC4-555-033330	101.790 216	20.942 716	16.218	14.420	13.828	17.923	16.773	17.021	16.130	15.738	33.183 423	864.694 662	24	202071849	eeeeeeeee
UCAC4-555-033335	101.795 353	20.945 481	11.554	11.266	11.224	11.589	11.466	11.478	11.559	11.677	34.961 871	860.006 732	24	202071849	AAeeeAAAe
UCAC4-555-033336	101.795 597	20.950 077	16.008	14.560	14.051	17.444	16.468	16.771	16.030	15.720	39.036 805	859.140 643	24	202071849	eeeeeeeee
UCAC4-555-033338	101.799 223	20.951 700	15.611	14.331	14.073	15.935	15.416	15.625	15.249	15.125	39.999 106	855.879 192	24	202071849	eeeeeeeee
UCAC4-555-033418	101.876 901	20.980 552	14.091	13.383	13.252	14.427	14.080	14.193	14.071	14.044	55.344 496	786.888 096	24	202068459	AAeeeAAAe
UCAC4-555-033420	101.876 908	20.972 664	12.859	11.979	11.702	13.485	12.948	13.181	12.839	12.712	48.289 514	788.011 635	24	202068459	AAeeeAAAe
UCAC4-555-033425	101.881 285	20.975 126	16.224	13.317	12.709	17.317	16.082	16.193	15.201	14.762	49.903 488	784.005 099	24	202068459	eeeeeeeee
...															

[a]The photometry flag indicator: A-APASS photometry; T-Tycho photometry; e-estimated with 2MASS photometry.
[b]The X and Y coordinate of star at time 0, time 0 is defined as cadence 1 (BJD-2455895.528) for K2.0, and cadence 102 (BJD-2455975.178) for K2.1.
[c]The channel number of which the star is observed.
[d]The given K2 ID of the star.

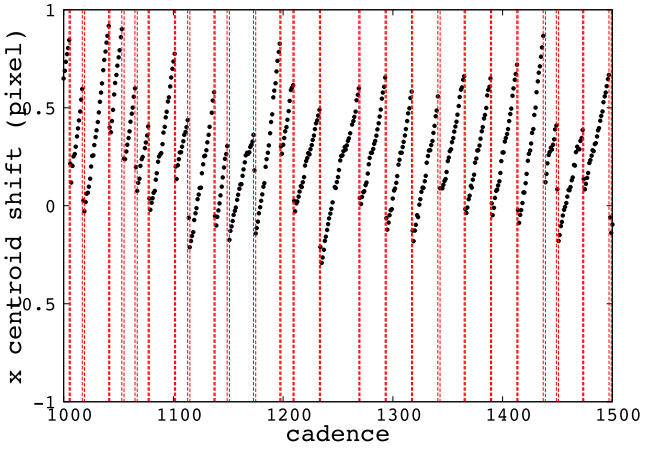

Figure 3. A segment of relative X centroid drift from module 4, between cadence 1000 and 1500. The dashed red lines separate the drifting segments we identified via edge detection.

taking the median, with iterative outlier rejection, in an annulus of pixels around the aperture, then multiplying it by the area of the aperture, and subtracting it from the flux. The aperture sizes range from 2.5 to 5 pixels, and are chosen so as to optimize the photometric precision for a wide range of magnitudes. For apertures with sizes smaller (larger) than 4.5 pixels, the background annulus has inner radii of 5 (6) pixels and outer radii of 11 (12) pixels. They are designed to optimize the photometric precision for stars in different magnitude bins. We note that for saturated stars (KepMag < 10), our photometric method cannot capture all the leaked electrons in the stamps, therefore leading to degraded photometry. For the saturated stars, the fixed aperture approach taken by VA14 remains the best way to extract optimized photometry for now.

4 LIGHT CURVES AND DETRENDING

We present the raw aperture photometry light curves (described in Section 3), and apply a three-step detrending process on our light curves. The detrending methodology is adapted from the HATNet pipeline, as well as the *Kepler* light-curve detrending pipeline described in Huang, Bakos & Hartman (2013). Each step of detrending is aimed to correct different aspects of the noise in the light curves. Users are able to query light curves detrended up to an intermediate step to suit their own purpose.[2] In this section, we will first describe the properties of our detrending methods, and then demonstrate the light-curve products from each detrending step. At the end of this section, we will compare our light curves with those from other works.

[2] http://k2.hatsurveys.org/

Table 2. Light-curve segments used in EPD.

Segment no.	Start cadence	End cadence
1	0	454
2	455	1005
3	1006	1989
4	2050	2314
5	2315	2997
6	2998	4020

4.1 Detrending

We refer to our light curves from the aperture photometry as RAWLC. Our detrending pipeline applied to these RAWLC can be divided into the following three steps:

(1) External Parameter Decorrelation (EPD);
(2) Trend filtering (TFA);
(3) Cosine filtering (COS).

To correct for the photometric variations due to the motion of the spacecraft, we performed EPD on the RAWLC (Bakos et al. 2010). We follow a similar methodology as described in VA14 to deal with the thrust fire events of the spacecraft. Instead of correcting for the drift effect due to a 6 h roll, we make use of the drifting pattern of each module we identified from Section 2.6. We first reject the data points that fall in between any drifting segments. We then divide the data into six segments before detrending, as defined in Table 2. These segments are designed to separate large amplitude flux offset in the data, and allowing each segments to be represented by low-order smooth functions. For each segment, we iteratively fit a third-order B-spline through the median magnitude of each drifting segment with 3σ outlier rejection until the fit converges. This long-term trend represented by the B-spline is then removed.

We then fit for the variation due to spacecraft drift as per the following:

$$\begin{aligned} f(m) = {} & c_0 + c_1 \sin(2\pi X) + c_2 \cos(2\pi X) \\ & + c_3 \sin(2\pi Y) + c_4 \cos(2\pi Y) \\ & + c_5 \sin(4\pi X) + c_6 \cos(4\pi X) \\ & + c_7 \sin(4\pi Y) + c_8 \cos(4\pi Y), \end{aligned}$$

in which, X, Y represent the relative X, Y drift of the module on which the target sits. The fitted X, Y trend is then removed from the original RAWLC, and the B-spline long-term trend added back in. This preserves the long-term trend while minimizing the effects of short-term spacecraft motion. The light curves at this stage is called EPDLC.

The shared systematics between the stars are then corrected using an adaptation of the TFA designed for *Kepler*. The idea of TFA is to select a set of template light curves, that is representative of all the systematic variations present in the data. Each target light curve is then corrected based on a linear filter that identifies the shared trends between the target and the template light curves. We found that using only template stars observed in the same channel as the target provided the best results. Since the number of stars observed in each channel in *K2* Campaign 1 is quite small, we use all the stars but the target as templates in the TFA procedure. The TFA filtered light curves are denoted as TFALC.

The last step is to filter all the low-frequency variabilities (mostly due to intrinsic stellar variability) using a set of cosine and sine functions. This method was implemented by Huang et al. (2013) for the independent search of planetary candidates in the original *Kepler* data. We aim to keep all periodicities at or below the protected time-scale of the transit undisturbed, while minimizing any other variations following Kipping et al. (2013). The cosine function detrending is applied to the EPDLC light curves, the resulting light curves are called the COSLC. The cosine function detrending process is independent of the TFA process above. Due to its purpose, astrophysical signals such as stellar pulsations are no longer preserved in the COSLC.

4.2 Light-curve products

We provide two types of measurements about the precision of our light curves. We use the point-to-point median scatter around the median (MAD) to represent the overall variability in the light curves which is used as an estimation of noise level in our transit search algorithm. We also report the 6.5 h precision as per VA14, which characterizes the noise of light curves at a time-scale relevant to the transit duration of an earth analogue. Fig. 4 shows the MAD of our light curves. The best precision of RAWLC, EPDLC, COSLC and TFALC for the bright stars are 1.2×10^{-4} (120 ppm), $\sim 6 \times 10^{-5}$ (60 ppm), $\sim 5 \times 10^{-5}$ (50 ppm) and $\sim 5 \times 10^{-5}$ (50 ppm), respectively. Fig. 5 shows the estimated 6.5 h precision of our light curves. The best precision of RAWLC for the bright stars are $\sim 2 \times 10^{-5}$ (20 ppm), and $\sim 1.5 \times 10^{-5}$ (15 ppm) for all the other three types of light curves. We also overlaid the estimation of the bottom envelop of the original *Kepler* 6.5 h precision based on Jenkins et al. (2010).

We show that the EPD process always improves both the short time-scale (6.5 h) and the long time-scale (whole campaign) precision compared to the RAWLC. We find a greater improvement for the bright stars compared to the faint stars. The COS filtering process improves the precision in both time-scales compared to EPDLC. For most stars, the TFALC has a similar or marginally worse precision compared with the COSLC, but the TFA process tends to preserve the intrinsic variabilities of the stars. We note that for a small fraction of the stars, the COSLC and TFALC can have a worse 6.5 h precision compared to the EPDLC. This is because the cosine filter and TFA algorithm both use linear least square method aiming to minimize the overall point-to-point scattering in the light curves, which is sometime achieved at the cost of increasing noise at specific time-scale. We compare the noise properties of the light curves in Fig. 6 by showing the ratio of per point root mean square (rms) and MAD versus magnitude. If the noise is composited with pure white noise, this ratio should be $\sqrt{2}$. The TFALC have the most white noise compared to other detrending stages.

5 COMPARISON WITH OTHER WORKS

Many teams have developed methods to improve *K2* photometry. We summarize the different approaches according to their photometry and detrending methods.

5.1 Photometry methods of previous works

All the teams use aperture photometry method to extract the light curves from *K2* data. However, they differ in the details of aperture choice and centroid measurements:

(i) Fixed mask method: The fixed mask method is such that the flux of the target is summed up over pixels within a fixed predetermined mask, while the pixels are accounted in a binary way.

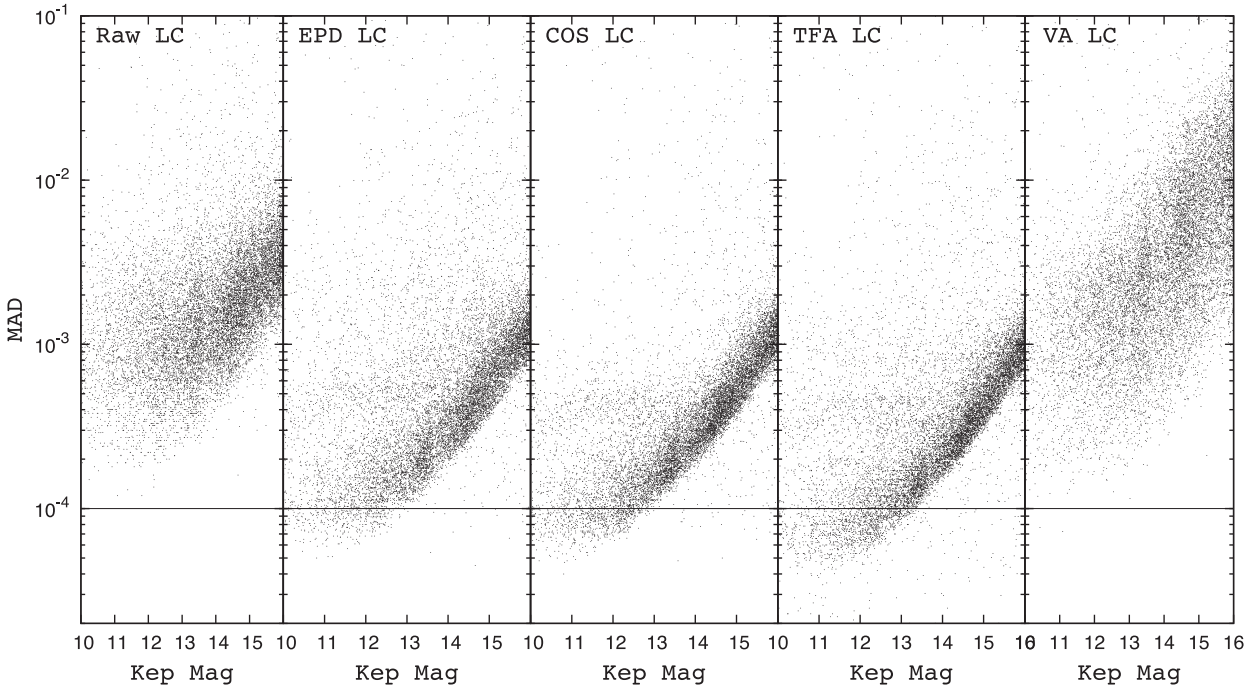

Figure 4. The point-to-point median standard deviation around the median (MAD) versus *Kepler* magnitude of all the light-curve products at different detrending stages. From left to right, we show the RAWLC the EPDLC, the COSLC the TFALC and the VALC. The solid horizontal line indicates a scatter of 10^{-4} (100 ppm). The vertical scale is logarithmic, and is the same for each panel.

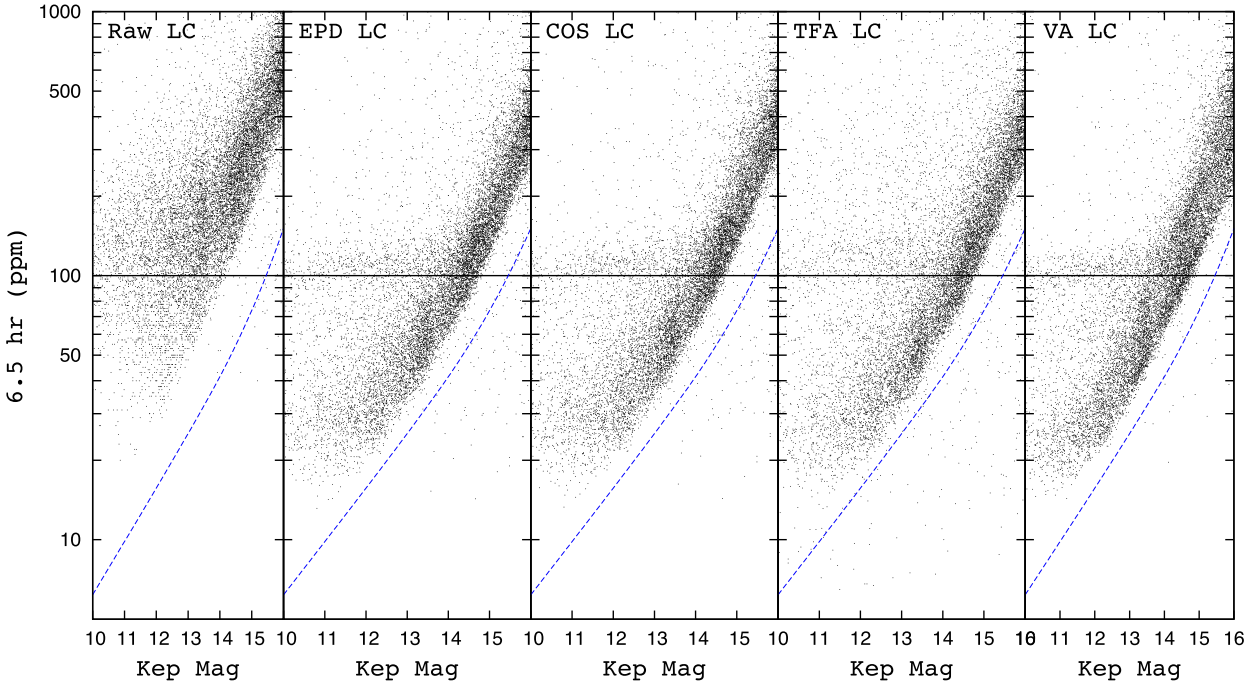

Figure 5. The 6.5 h precision versus *Kepler* magnitude of all the light-curve products at different detrending stages. From left to right, we show the RAWLC the EPDLC, the COSLC the TFALC and the VALC. The solid black horizontal line indicates a scatter of 10^{-4} (100 ppm). The vertical scale is logarithmic, and in units of parts per million (ppm). The dashed blue line is the fitted function indicate the bottom envelope of the original *Kepler* 6.5 h precision based on Jenkins et al. (2010).

VA14 used a combination of approximate circular aperture and fitted apertures using the *Kepler* Pixel Responding Function (Bryson et al. 2010). Foreman-Mackey et al. (2015) and Angus et al. (2015) used approximate circular but binary apertures (do not include pixels partially) and present the photometry from the best apertures. Lund et al. (2015) used the density-based spatial clustering of applications with noise routine (DBSCAN; Ester et al. 1996) to chose their pixel mask (aperture).

(ii) Moving circular aperture method: Aigrain et al. (2015) used six circular apertures to extract photometry. The apertures are

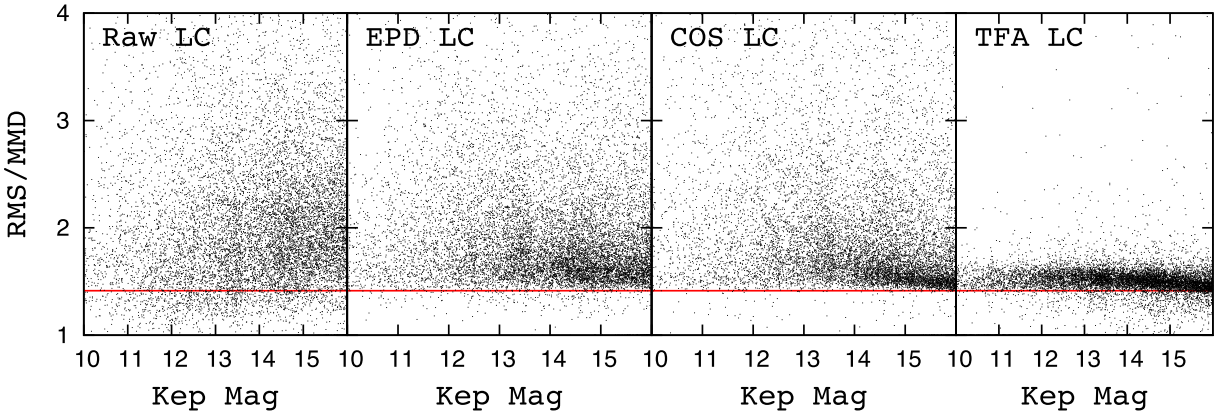

Figure 6. Ratio of point-to-point RMS and MAD versus *Kepler* magnitude. From left to right, we show the RAWLC the EPDLC, the COSLC and the TFALC. The red horizontal line indicates the value of $\sqrt{2}$, which should be the value or their ratio for pure white noise.

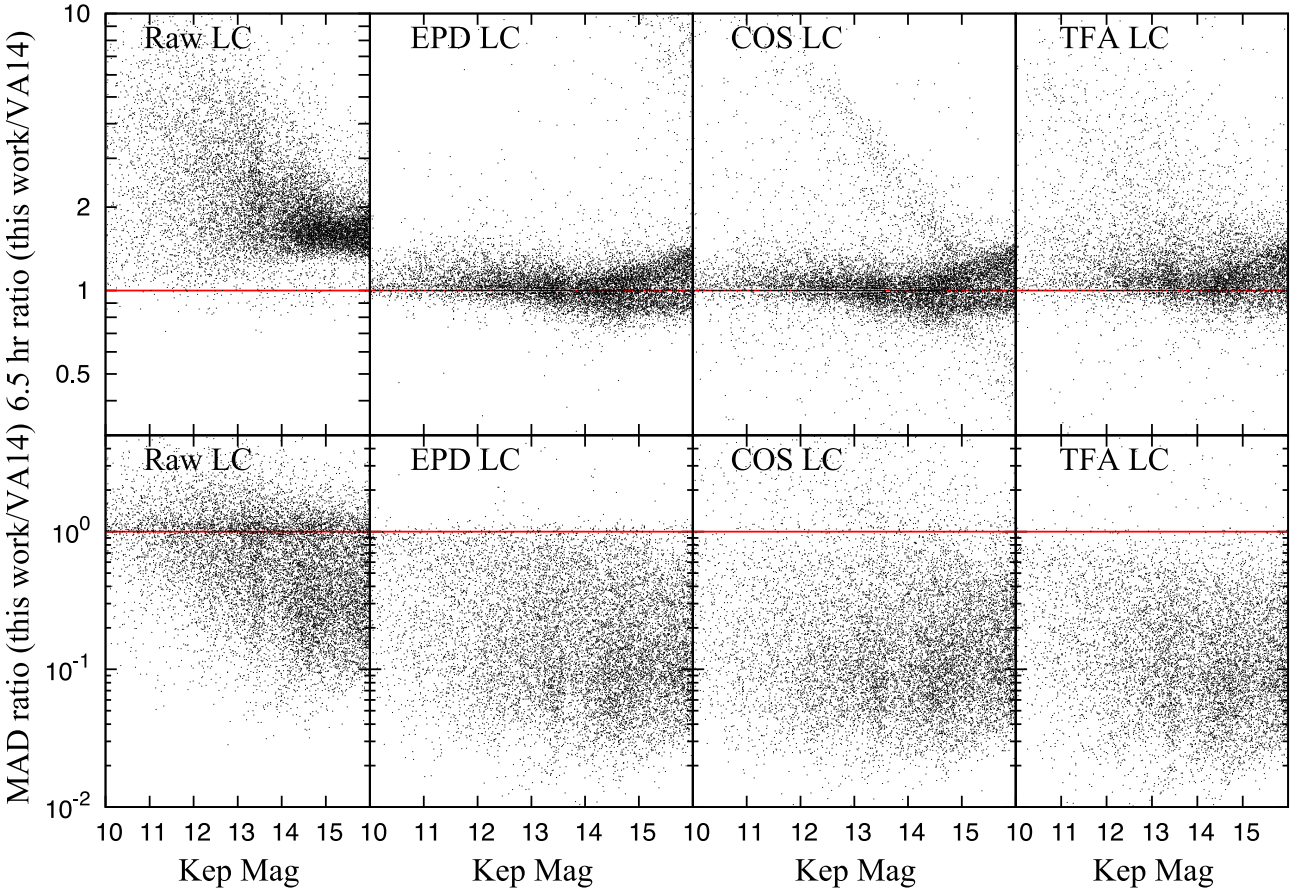

Figure 7. Photometry precision of our light curves compared to VA14 *K2* Campaign 1 light curves. Top panel: 6.5 h precision ratio between our light curves and VA14 light curves versus *Kepler* magnitude. Bottom panel: per point MAD ratio between our light curves and VA14 light curves versus *Kepler* magnitude. From left to right, we show the RAWLC the EPDLC, the COSLC and the TFALC. The red horizontal line indicates the value of 1. We note the vertical scale in the two panels are different, and both in log scale.

soft-edged, in the sense that pixels straddling the edge of the aperture contribute partially to the flux.

(iii) Centroids from astrometric solution: Aigrain et al. (2015) used centroids derived from their own astrometric solution with the 2MASS all-sky point-source catalogue.

(iv) Centroids from WCS header: Foreman-Mackey et al. (2015) and Angus et al. (2015) used centroids from the WCS header of the *K2* target pixel files. Only one WCS solution is given for the entire time series of each star.

(v) Centroids from weighted centre of flux: VA14 and Lund et al. (2015) used the weighted centre of flux as the centroids of the stars. We note, in the subsequent detrending, VA14 used the centroid of star EPIC 201611708 instead of the centroids of individual stars.

In this work, we used 36 moving circular apertures, with the centroids of apertures determined by precise astrometric solutions, to determine the photometry of each star.

5.2 Detrending methods of previous work

There are three different types of 'detrending' methods used by other authors.

(i) Decorrelation: VA14, Armstrong et al. (2015) and Lund et al. (2015) used a self-flat-field method to decorrelate the aperture photometry from centroid position of the image. There are, however, subtle differences between these studies. VA14 used the centroids from a representative star, Armstrong et al. (2015) seemed to use centroids for individual stars, while Lund et al. (2015) used the weighted light centroids derived for individual stars. VA14 used a 1D decorrelation along the trajectory of the drift, Armstrong et al. (2015) used 2D centroid surface to decorrelate with the flux, and Lund et al. (2015) used both the 1D and 2D approach in their pipeline.

(ii) Gaussian process: Aigrain et al. (2015) and Crossfield et al. (2015) used Gaussian process model, with the rolling angle as the input variable to detrend the light curves. They assume the systematics can be modelled as a function form of the rolling angle, and that function's form can vary from star to star.

(iii) Not detrending: Foreman-Mackey et al. (2015) and Angus et al. (2015) choose to not detrend their light curve prior to the search of signal, but instead, they simultaneously fit for the systematics and the signal of interest.

In this work, we applied three stages of detrending. In the first stage, we applied a similar method as the decorrelation detrend in VA14. We additionally applied TFA and COS filtering to further filter the data. TFA is aimed to correct for shared systematics between the stars observed on the same channel, while preserving the stellar variability. The COS filtering method aimed to correct for any variability in the light curves and is optimized for searching for transit signals.

5.3 Centroids determination

We took a similar approach as Aigrain et al. (2015) in the determination of centroids by deriving an astrometric solution for each image. We made use of a more precise catalogue, UCAC4 instead of 2MASS, and the Full Frame Image as a better initial guess, and achieved higher precision in our astrometric solution. Aigrain et al. (2015) reported a typical root mean square of the astrometric solution of 0.4 arcsec, or approximately 0.1 pixel, ∼3 times larger than our typical astrometric residuals.

5.4 Photometric precision

To date, only VA14 have released their detrended *K2* Campaign 1 light curves, therefore we will focus on comparing our photometry precision with their work.

We show in Fig. 7 the precision ratio between our light curves and the VA14 light curves, for the same stars at both times scales. The EPDLC, COSLC and TFALC from this work have comparable precision compare to VA14 light curves on the 6.5 h time-scale, and a smaller point-to-point scatter over the entire observation length.

Aigrain et al. (2015) presented their $\sigma_{\rm MAD}$ (similar to MAD) and 6.5 h Combined Differential Photometric Precision (CDPP) for *K2* engineering data photometry. Their best precision for $\sigma_{\rm MAD}$ is

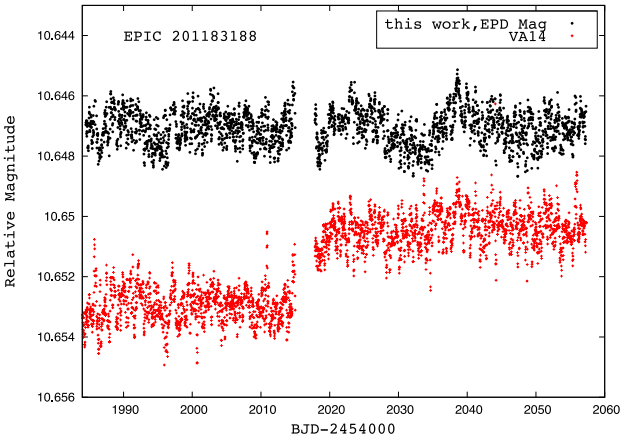

Figure 8. The EPDLC for EPIC 201183188 from this work (black), and VA14 (red). The DFT power spectrum of this star is shown in Fig. 9.

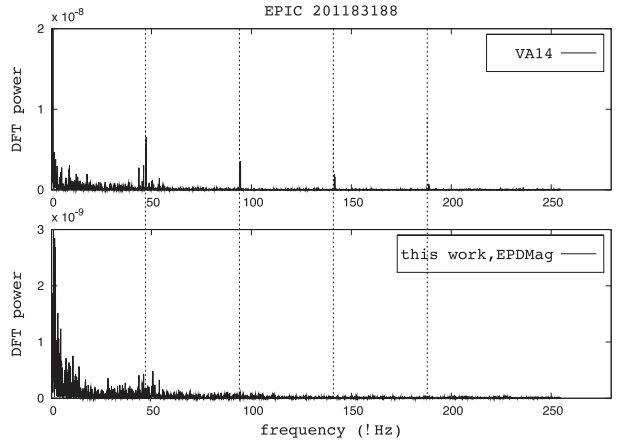

Figure 9. The DFT power spectrum for EPIC 201183188 from this work (top panel) and VA14 (bottom panel). Note the vertical scales are different in the two panels. The dash lines indicate the corresponding frequency associated with the spacecraft roll motion. For more discussion, see Angus et al. (2015).

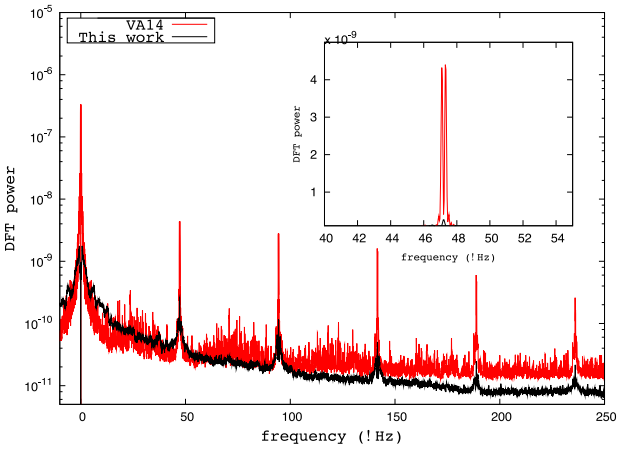

Figure 10. The median DFT power spectrum of 1661 stars in the magnitude range 10–12. Red dashed lines show the result from the VA14 light curves. Black solid lines show the result from the EPDLC of this work. In the small window of this figure, we show the zoom-in of these spectra around the space craft roll frequency ∼47.2271 μ Hz.

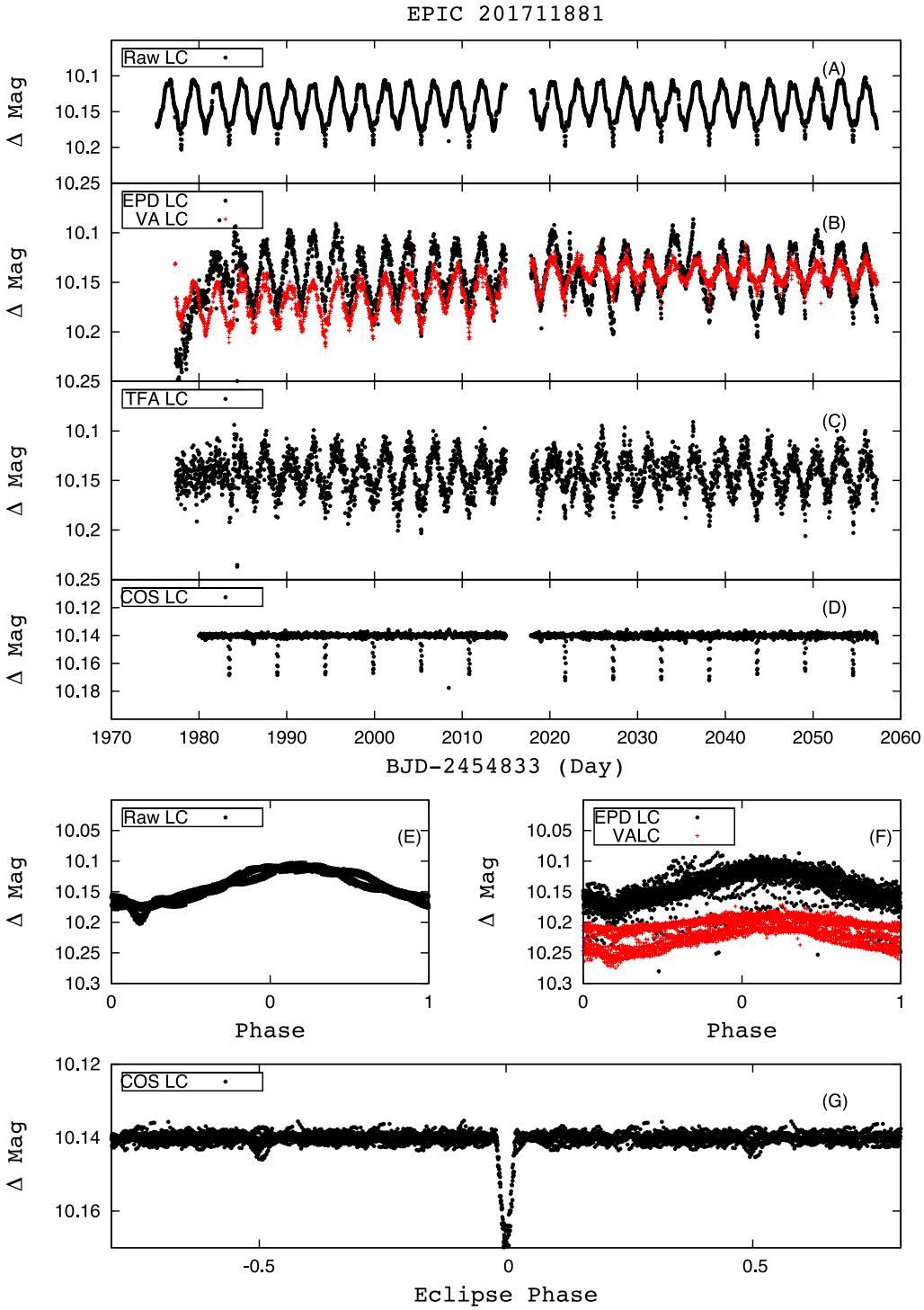

Figure 11. The light curves of EPIC 201711881, a Cepheid Candidate discovered by Schmidt et al. (2009). From the top to bottom, we show the RAWLC (A), EPDLC (B), TFALC (C) and COSLC (D). In panel (E) and (F), we show RAWLC and EPDLC folded with the period of the pulsation period (∼2.735 d) in the phase space. The last panel we show COSLC (G) folded with twice the period of the pulsation. The eclipse events can be seen at phase 0. The COSLC in panel (D) and (E) have been reconstructed after the discovery of the eclipsing signal. Only the out-of-eclipse part have been filtered by the cosine filters in order to preserve the signal. The red light curve in figure (B) and (F) is from VA14. We note that the vertical scales are different for each panel.

∼ 300 ppm for the bright stars, and 60 ppm for 6.5 h CDPP. In this work, we achieved higher precision on both time-scales (50 and 15 ppm, respectively). Although, we caution that the noise characteristic for *K2* engineering data and *K2* Campaign 1 data could be different.

5.5 Power spectrum

Previous works (Angus et al. 2015; Lund et al. 2015) noted the detrended light curves from a 1D decorrelation may still have residual spikes around the harmonics of ∼47.2271 μHz in their power

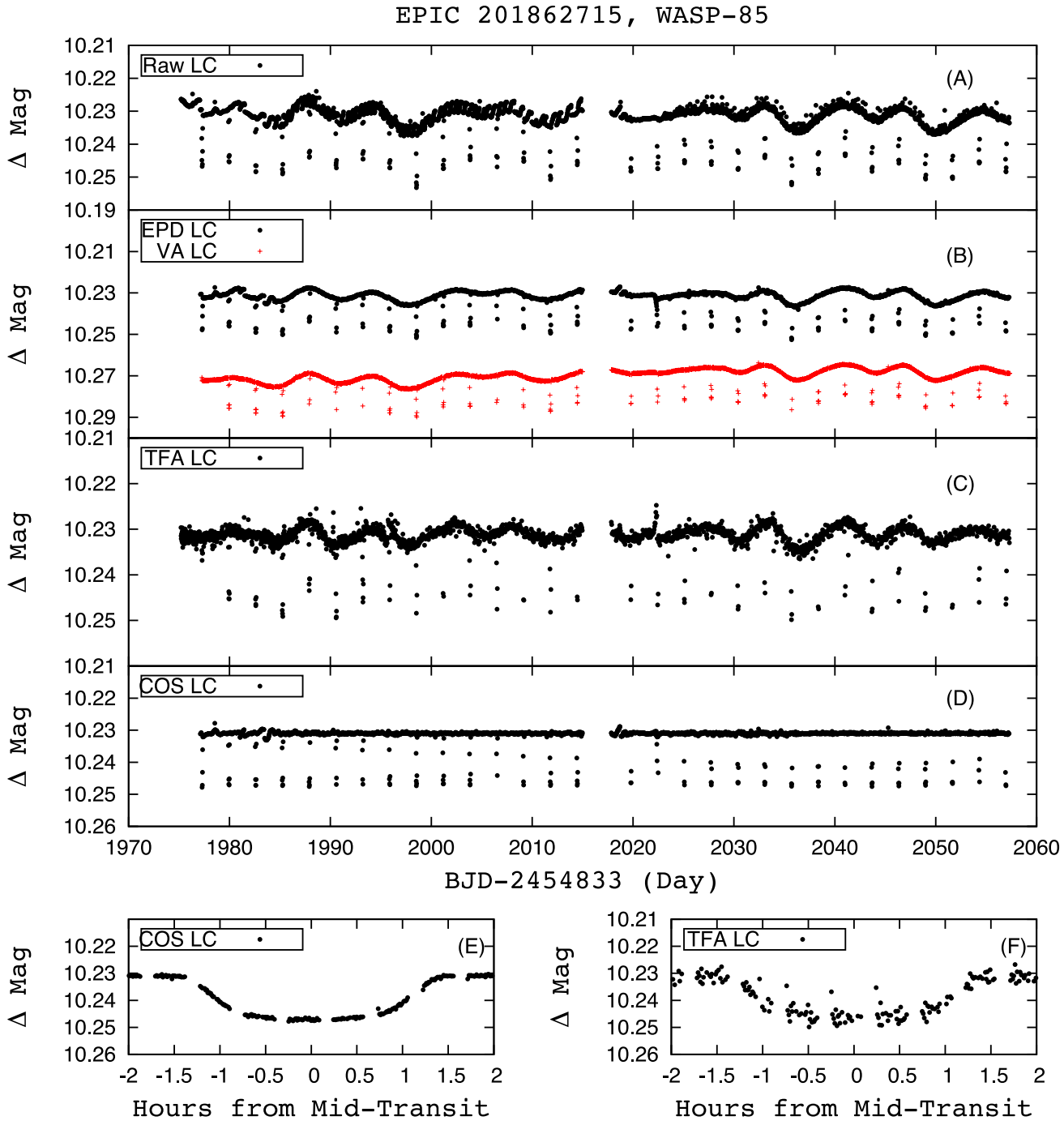

Figure 12. The light curves of WASP85 (black). From the top to bottom, we show the RAWLC, EPDLC, TFALC and COSLC. The bottom most panel, we show COSLC and TFALC of WASP85 folded with the epoch and period of WASP-85b (Brown et al. 2014). The red light curve in the second panel is from VA14. We note that the vertical scales in different panels are different.

spectra. These residuals may be largely due to aliasing of the low-frequency power, induced by data gaps from rejected points during thruster firing. These harmonics are less obvious in our light curves.

We computed the Discrete Fourier Transformation (DFT) power spectrum using VARTOOLS (Hartman et al. 2008) for the star EPIC 201183188, following Angus et al. (2015). We find our EPDLC does not show the frequencies corresponding to the 6 h roll in the DFT power spectrum present in the VA14 light curves. Fig. 8 compares our EPDLC for EPIC 201183188 with the VA14 reduction, and Fig. 9 compares the DFT power spectrum of our EPDLC with that of the VA14 light curve. The offset around epoch BJD 2456015 in the VALC could be blamed for contributing to noise peaks corresponding to the space craft rolling frequency.

We further investigate the noise characteristic of the light curves by computing the median of DFT power spectra of 1661 stars in the magnitude range of 10–12. To eliminate the influence from the long-term trend, we first filter out the strongest low-frequency peak in the light curves, and then recompute the DFT power spectra of each star before taking the median. We show this median spectrum in Fig. 10. The peaks related to the rolling frequency are still present, but have

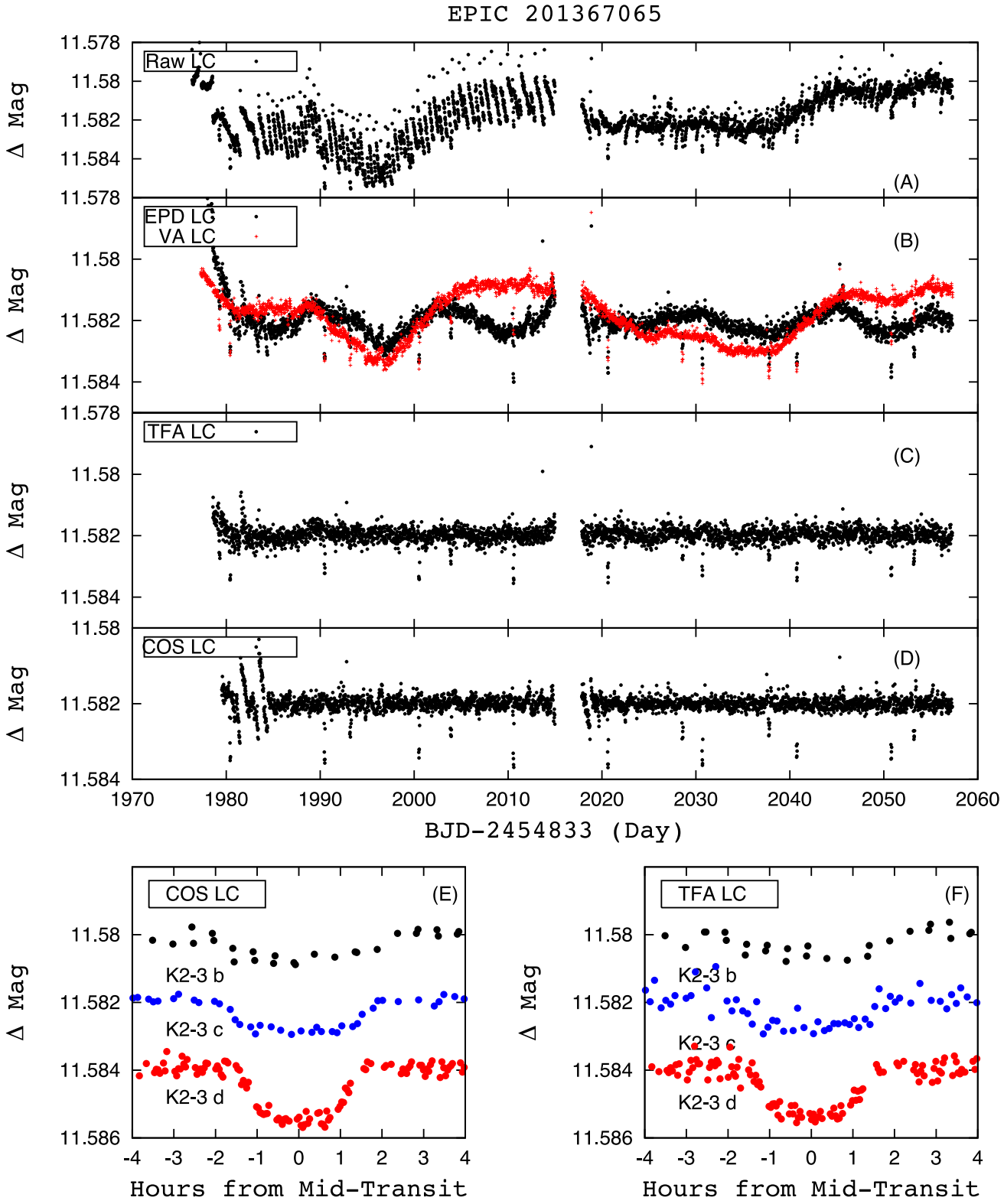

Figure 13. Same as Fig. 12, but for K2–3 (Crossfield et al. 2015). In the bottom panel, we show all the three planets detected in this system folded with their own periods and epochs. K2–3 b (P∼ 10 d, R∼2$R_\oplus$), c (P∼ 25 d, R∼1.7$R_\oplus$), d (P∼ 44 d, R∼1.5 $R_\oplus$) are presented in red,blue and black curves, respectively. We note that the vertical scales in different panels are different.

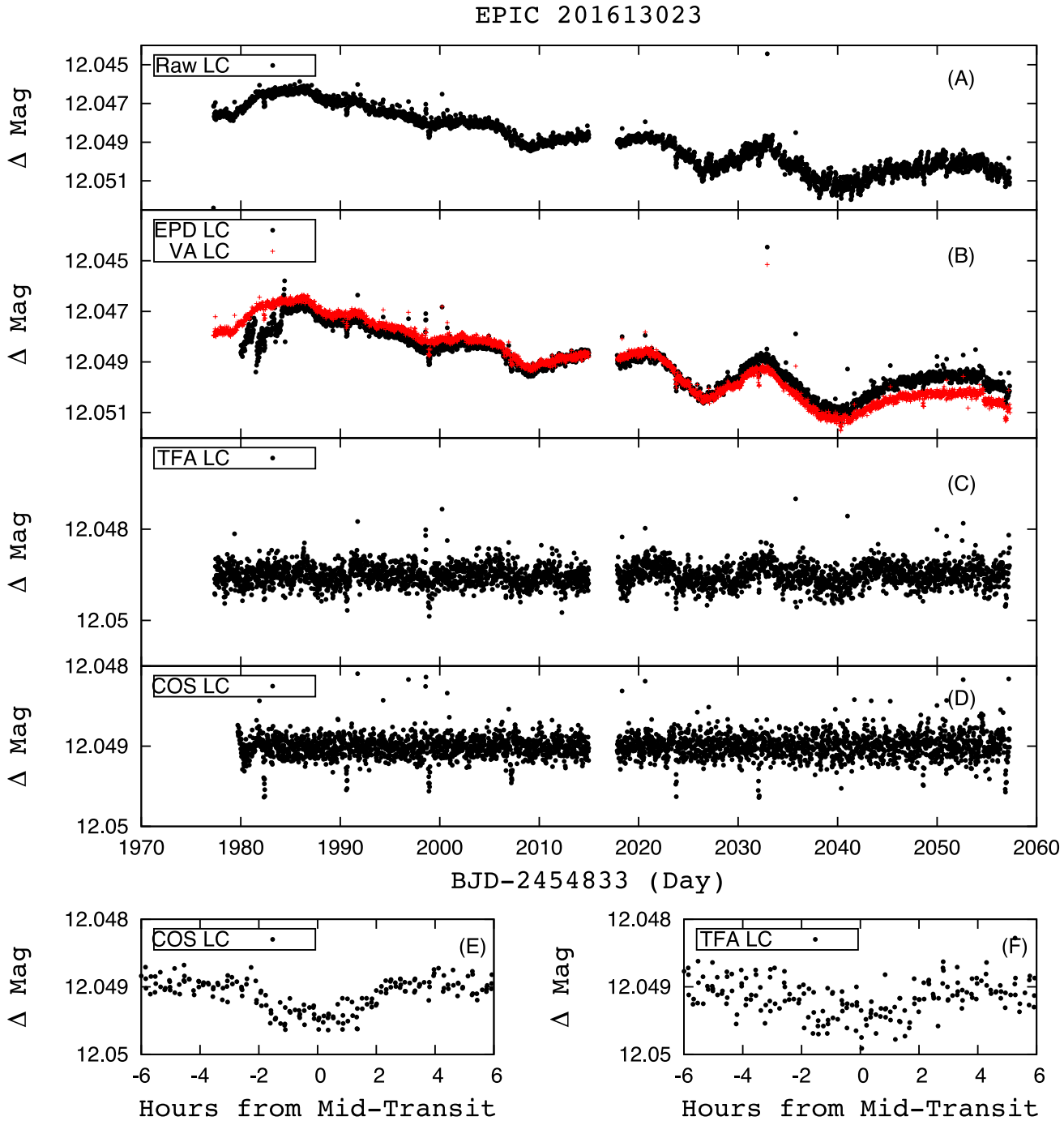

Figure 14. Same as Fig. 12, but for EPIC 201613023 (Foreman-Mackey et al. 2015). In the bottom panel, we show the detected planet candidate folded with its period (∼8.28 d). The depth of the transit is ∼ 400 ppm. We note that the vertical scales in different panels are different.

less power compared to the median DFT spectrum computed with the same set of stars from VA14. When the signal from stellar variability is strong, such as in the case of EPIC 201183188, the systematic noise peaks are negligible.

5.6 Example light curves

To demonstrate the products of our photometric extraction and detrending in the context of stellar variability and transit searches, we show example light curves for stars with known variability and transiting signals.

EPIC 201711881, is a Cepheid candidate discovered by the ASAS project (Schmidt et al. 2009). The original discovery paper reported a period of $2.7353 \pm 5 \times 10^{-4}$ d. The period we detected is ∼2.735 d, consistent with (Schmidt et al. 2009). The RAWLC and EPDLC folded with the Cepheid period, are shown in Fig. 11. Our RAWLC without any detrending, already shows a clean periodic signal. In addition, our EPDLC preserves the amplitude of the pulsation after removing the systematics. We also find a periodic eclipsing signal in the light curve with twice the pulsation period. This eclipsing signal can be visually seen, even in the RAWLC. The COSLC, phase folded with the eclipse period, is also plotted in the

bottom panel of Fig. 11. It seems that this system is more likely to be an eclipsing binary system with large out-of-transit variation rather than a real Cepheid. To further characterize this signal, the COSLC from the general detrending pipeline is not good enough. The COSLC we show in Fig. 11 have been reconstructed after the discovery of the eclipsing signal. Only the out-of-eclipse part have been filtered by the cosine filters in order to preserve the shape and amplitude of the eclipsing signal.

WASP-85b: WASP-85 (EPIC 201852715), was observed in *K2* Campaign 1, in module 15, channel 49. 1182 other stars were observed in the same module. We show in Fig. 12 the light curves of WASP-85 at different detrending stages from this work. In the second panel from the top, we also overlaid the VA14 detrended light curve. WASP-85b has a period of ∼2.65 d, and known depth of ∼1.6 per cent. We show the WASP-85 light curve folded with the detected period and epoch in phase space for both the COSLC and TFALC in the bottom of Fig. 12.

K2–3: K2–3 (EPIC 201367065), was observed in *K2* Campaign 1, in module 12, channel 40. The host star is an M dwarf, with three transiting super-Earths discovered by Crossfield et al. (2015). We show the light curves for K2–3 in Fig. 13. The transits of the biggest planet (1 mmag) is visible in our RAWLC, and the transits of all three planets are visible in all the other light curves. We also show the phase folded COSLC and TFALC for all three planets in the bottom panel of Fig. 13.

EPIC 201613023: this star was identified as a transiting planet candidate system by Foreman-Mackey et al. (2015). We show our light curves in Fig. 14. The transit signal has depth of 400 ppm. Individual transits from the planets are visible in the EPDLC, TFALC and COSLC. The phase folded COSLC and TFALC with the detected epoch and period are shown in the bottom panel.

6 CONCLUSION AND DISCUSSION

In this article, we present our effort to extract high-precision photometry from *K2* Campaign 1 data. Our method has three distinct advantages:

(i) making use of accurate astrometric solution (0.127 arcsec or 0.034 pixels) from the FFIs for aperture centroiding;
(ii) providing photometry for all sources on the stamps, not only for the proposed targets from the input catalogue;
(iii) presenting light curves with very low systematic variations.

Our extracted light curves are of high precision at both the long (entire campaign) and short (6.5 h) time-scales, even for the raw light curves without any detrending. Light curves derived from all 36 photometric apertures at all four detrending stages are provided for the public at http://k2.hatsurveys.org.

ACKNOWLEDGEMENTS

We would like to thank the referee for their helpful comments. We also thank AV for his thoughtful suggestions. GB and XH acknowledge funding from the Packard Foundation. This work was also supported by NASA grant NNX13AJ15G. KP acknowledges support from NASA grant NNX13AQ62G. The *K2* data presented in this paper were obtained from the Mikulski Archive for Space Telescopes (MAST). STScI is operated by the Association of Universities for Research in Astronomy, Inc., under NASA contract NAS5-26555. Support for MAST for non-*HST* data is provided by the NASA Office of Space Science via grant NNX09AF08G and by other grants and contracts. This paper includes data collected by the *Kepler* telescope. Funding for the *K2 Mission* is provided by the NASA Science Mission directorate.

REFERENCES

Ahn C. P. et al., 2012, ApJS, 203, 21
Aigrain S., Hodgkin S. T., Irwin M. J., Lewis J. R., Roberts S. J., 2015, MNRAS, 447, 2880
Angus R., Foreman-Mackey D., Johnson J. A., 2015, preprint (arXiv:e-prints)
Armstrong D. J. et al., 2015, A&A, 579, A19
Bakos G. Á. et al., 2010, ApJ, 710, 1724
Bertin E., Arnouts S., 1996, A&AS, 117, 393
Brown D. J. A. et al., 2014, preprint (arXiv:e-prints)
Bryson S. T. et al., 2010, ApJ, 713, L97
Crossfield I. J. M. et al., 2015, ApJ, 804, 10
Ester M., Kriegel H.-p., Sander J., Xu X., 1996, AAAI Press, 226
Foreman-Mackey D., Montet B. T., Hogg D. W., Morton T. D., Wang D., Schölkopf B., 2015, ApJ, 806, 215
Hartman J. D., Gaudi B. S., Holman M. J., McLeod B. A., Stanek K. Z., Barranco J. A., Pinsonneault M. H., Kalirai J. S., 2008, ApJ, 675, 1254
Howell S. B. et al., 2014, PASP, 126, 398
Huang X., Bakos G. Á., Hartman J. D., 2013, MNRAS, 429, 2001
Huber D., Bryson S. T., 2015, KSCI-19082-008
Høg E. et al., 2000, A&A, 355, L27
Jenkins J. M. et al., 2010, ApJ, 713, L120
Kipping D. M., Hartman J., Buchhave L. A., Schmitt A. R., Bakos G. Á., Nesvorný D., 2013, ApJ, 770, 101
Lang D., Hogg D. W., Mierle K., Blanton M., Roweis S., 2010, AJ, 137, 1782
Lund M. N., Handberg R., Davies G. R., Chaplin W. J., Jones C. D., 2015, ApJ, 806, 30
Monet D. G., Jenkins J. M., Dunham E. W., Bryson S. T., Gilliland R. L., Latham D. W., Borucki W. J., Koch D. G., 2010, preprint (arXiv:e-prints)
Pál A., 2012, MNRAS, 421, 1825
Schmidt E. G., Hemen B., Rogalla D., Thacker-Lynn L., 2009, AJ, 137, 4598
Skrutskie M. F. et al., 2006, AJ, 131, 1163
ed.van Leeuwen F., 2007, Astrophysics and Space Science Library, Vol. 350, Hipparcos, the New Reduction of the Raw Data. Springer, Berlin
Vanderburg A., Johnson J. A., 2014, PASP, 126, 948
Zacharias N., Finch C. T., Girard T. M., Henden A., Bartlett J. L., Monet D. G., Zacharias M. I., 2013, AJ, 145, 44

This paper has been typeset from a TEX/LATEX file prepared by the author.